NANO LETTERS

pubs.acs.org/NanoLett Letter

Topological Surface State Annihilation and Creation in SnTe/$Cr_x(BiSb)_{2-x}Te_3$ Heterostructures

Peng Deng,* Alexander Grutter, Yulei Han, Megan E. Holtz, Peng Zhang, Patrick Quarterman, Shuaihang Pan, Shifei Qi, Zhenhua Qiao,* and Kang L. Wang*

Cite This: *Nano Lett.* 2022, 22, 5735−5741 Read Online

ACCESS | Metrics & More | Article Recommendations | Supporting Information

ABSTRACT: Topological surface states are a new class of electronic states with novel properties, including the potential for annihilation between surface states from two topological insulators at a common interface. Here, we report the annihilation and creation of topological surface states in the SnTe/$Cr_x(BiSb)_{2-x}Te_3$ (CBST) heterostructures as evidenced by magneto-transport, polarized neutron reflectometry, and first-principles calculations. Our results show that topological surface states are induced in the otherwise topologically trivial two-quintuple-layers thick CBST when interfaced with SnTe, as a result of the surface state annihilation at the SnTe/CBST interface. Moreover, we unveiled systematic changes in the transport behaviors of the heterostructures with respect to changing Fermi level and thickness. Our observation of surface state creation and annihilation demonstrates a promising way of designing and engineering topological surface states for dissipationless electronics.

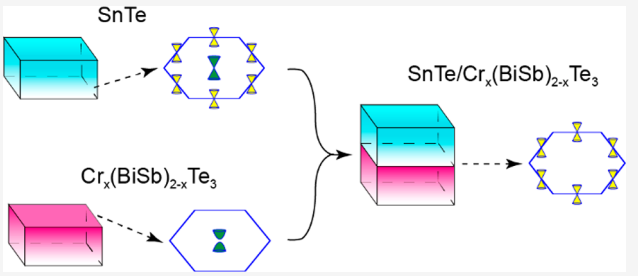

KEYWORDS: *magnetic topological insulators, topological crystalline insulators, surface state annihilation, anomalous Hall effect, polarized neutron reflectometry*

Topological insulators (TIs) have received much attention as a new class of topologically nontrivial materials that are bulk insulators with conductive states on the surfaces.[1,2] These surface states are symmetry-protected and appear at the interface between the TI and any topologically trivial media, so that their existence is maintained even in the presence of surface defects. Although such robustness against perturbations is highly desirable in the pursuit of devices based on dissipationless transport, it presents serious challenges in the endeavor to tailor the surface states, particularly for the implementation of TI-based spintronics. Yet the topological nature of surface states also offers a unique way to engineer their properties in TI heterostructures: surface states from two different TIs could annihilate each other at a common interface if they have the same spin chirality.[3]

The TI heterostructure, particularly the TI/magnetic TI (MTI) heterostructure, provides a platform to realize various topological phenomena, such as quantum anomalous Hall effect (QAHE),[4,5] half-integer QAHE,[6] topological Hall effect,[7,8] exchange bias,[9] etc. While, in these TI bilayers or superlattices, the properties of the system can be tuned by multiple parameters, the idea of surface state annihilation is less discussed or appreciated. One reason is that in these systems, TI and MTI belong to the same topology class; one cannot assess the results of surface state annihilation given the similarity between TI and MTI. Interestingly, the annihilation of surface states can also occur between TIs with different symmetry protections, e.g., between Bi_2Te_3 and SnTe. Bi_2Te_3 is a Z_2 TI with a Dirac cone at the $\bar{\Gamma}$ point of the surface Brillouin zone,[10−13] while SnTe is a topological crystalline insulator and its surface states form one Dirac cone at the $\bar{\Gamma}$ point and three Dirac cones at the $\bar{M}$ points on the (111) surface.[14−19] Tight-binding calculations predict that, at the common interface, two surface states at the $\bar{\Gamma}$ points of Bi_2Te_3 and SnTe, respectively, hybridize and merge into bulk states.[3] That is, these two topological surface states annihilate each other. The surface states at the $\bar{M}$ points, strikingly, remain intact and survive at the interface. Such annihilation fundamentally changes the number of surface states, altering the electronic properties of the heterostructure system. While surface state interaction at TI interfaces is a subject of enormous interest in theory,[3,20−22] experimental studies have been very limited to date.

Here, we examine the interaction between the surface states of SnTe and $Cr_x(BiSb)_{2-x}Te_3$ (CBST) by carrying out magneto-transport and polarized neutron reflectometry (PNR) experiments on the SnTe/CBST heterostructures.

Received: February 24, 2022
Revised: May 30, 2022
Published: July 19, 2022

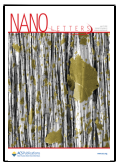

https://doi.org/10.1021/acs.nanolett.2c00774
Nano Lett. 2022, 22, 5735−5741

Doping Cr introduces ferromagnetism into $(BiSb)_2Te_3$. While the ferromagnetism opens an exchange gap at the Dirac cone, the surface states still exist above a certain critical thickness. In an extremely thin CBST layer, however, its top and bottom surface states hybridize and prevent the formation of conductive states,[23−25] yielding a trivial insulator. However, if the top surface state of CBST is annihilated by a surface state of another TI interfacing with it, the hybridization will be eliminated, and the bottom surface state will form in CBST. With magneto-transport, we can directly probe the presence or the absence of a conductive magnetic surface state. Taking advantage of the magnetic sensitivity of the PNR along the film normal direction, we locate the magnetic surface state within the CBST layer, demonstrating the annihilation of topological surface states at the SnTe/CBST interface.

Figure 1a shows a cartoon of the lattice structure of the heterostructure. The CBST films were grown on GaAs(111)B

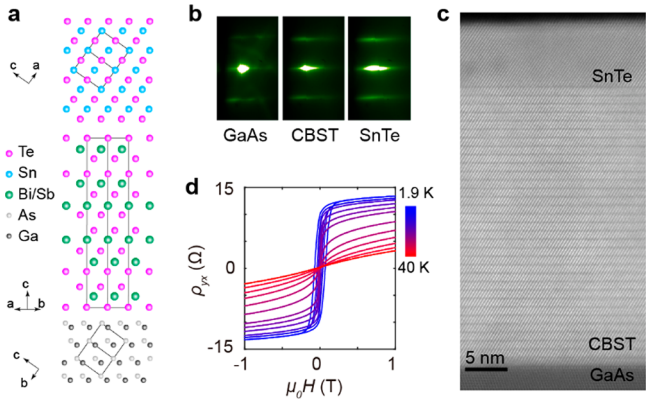

Figure 1. Growth and characterization of SnTe/CBST heterostructure. (a) Lattice structure of the SnTe/CBST heterostructure on GaAs substrate. (b) RHEED patterns of GaAs, CBST, and SnTe along [$\bar{1}$10], [110], and [$\bar{1}$10] directions, respectively. (c) STEM image of the SnTe/CBST heterostructure. (d) Field dependence of ρ_{yx} for a 14-BL-SnTe/2-QL-CBST sample.

substrates using molecular beam epitaxy (MBE). SnTe (111) layers were subsequently grown on top of CBST with an ∼1% lattice mismatch.[26−28] Figure 1b presents the reflection high-energy electron diffraction (RHEED) patterns of the GaAs, CBST, and SnTe surfaces, where the flatness of these surfaces is revealed by the streaky patterns along [$\bar{1}$10], [110], and [1$\bar{1}$0] directions, respectively. Nanobeam electron diffraction shows relaxed films with the expected relative epitaxial relationships (Supporting Information Figure S1). The quality of the films is further confirmed by scanning transmission electron microscopy (STEM) measurements. As shown in Figure 1c, an atomically sharp interface between SnTe and CBST is clearly seen in a 22-bilayer (BL)-SnTe/32-quintuple layer (QL)-CBST sample. The sharp interface is also observed by electron energy-loss spectroscopy (EELS) and X-ray energy dispersive spectroscopy (XEDS), as shown in Figure S2.

MBE-grown films were patterned into Hall bars for transport measurements, in which the thickness of the CBST layer is 2 QL for all samples. Since the 2 QL CBST is below the thickness limit of three-dimensional TI (4 QL),[29] it is a trivial insulator. As expected, the bare 2 QL CBST film is highly insulating at low temperatures with a resistance over 20 MΩ at 10 K (Figure S4a). In contrast, the sample becomes conductive after growing 14 BL SnTe on top (Figure S4b). Figure 1d presents the field dependence of the Hall resistance (ρ_{yx}) for the 14-BL-SnTe/2-QL-CBST sample. The hysteretic anomalous Hall (AH) data indicate the presence of ferromagnetism in the heterostructure at low temperatures.

The observed ferromagnetic order has two possible origins. If the CBST layer remains insulating after the deposition of SnTe and consequently does not contribute signal in the transport, then the hysteretic signal must come from the magnetization of the SnTe surface through the magnetic proximity effect.[30−33] In this circumstance, as illustrated in Figure 2a, ferromagnetism exists in both CBST and SnTe layers, while the transport probes only SnTe. Figure 2b shows the other possible scenario, in which there is no magnetic proximity effect and the magnetic signal stems from a surface state induced in the CBST. Although a 2QL CBST layer is

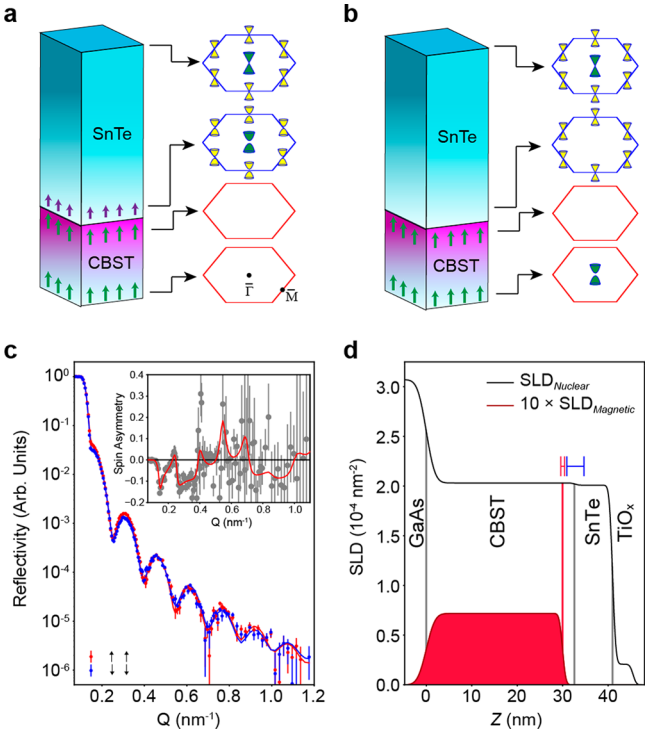

Figure 2. Magnetic proximity effect vs surface state annihilation. (a, b) Schematic illustrations of two possible scenarios in the SnTe/2-QL-CBST heterostructures. The distributions of the topological states in the surface Brillouin zones are shown on the right for both cases. While both scenarios can result in the observed magnetic hysteresis, in scenario a, the magnetic hysteresis arises from the topological states in the SnTe bottom, which are magnetized by CBST through a magnetic proximity effect. In this case, the 2-QL-CBST itself does not form topological surface states due to hybridization. In scenario b, there is no proximity effect and the hysteresis signal comes from CBST. The topological state at the $\bar{\Gamma}$ point of the SnTe bottom annihilates the hypothetical surface state on the top surface of CBST, lifting the hybridization in CBST; therefore, a topological state survives on the bottom surface of CBST. (c) PNR data of a 22-BL-SnTe/32-QL-CBST collected at 5 K with an applied in-plane field of 3 T. Inset: Spin asymmetry of the sample. Solid lines are theoretical fits to the data. Error bars correspond to ±1 standard deviation. (d) Nuclear and magnetic scattering length density profiles used to generate the theoretical curves shown. The red and blue highlighted regions represent 95% confidence intervals on the magnetic layer thickness and CBST thicknesses, respectively, showing the absence of the magnetic proximity effect between CBST and SnTe.

https://doi.org/10.1021/acs.nanolett.2c00774
Nano Lett. 2022, 22, 5735−5741

nominally topologically trivial due to the hybridization of the top and bottom surface states, growing a SnTe layer on top of it may annihilate the hypothetical top surface state of CBST, removing the hybridization and thus stabilizing the topological state on the bottom surface of CBST. In this scenario, ferromagnetism exists in the CBST layer only.

To differentiate between these two interpretations, we acquired a depth-resolved profile of the magnetization in the SnTe/CBST heterostructure using PNR. Through the nuclear and magnetic scattering factors, PNR is sensitive to the magnetic and chemical depth profile in thin film heterostructures, so that the spin-polarized reflectivity may be fit to extract information on which layers are magnetized and address the presence or absence of a magnetic proximity effect. Therefore, we performed PNR on a 22-BL-SnTe/32-QL-CBST sample at 5 K with an in-plane applied field of 3 T. Thicker SnTe and CBST layers were selected in PNR measurements in order to provide a more definitive answer regarding the presence or absence of a magnetic proximity-induced magnetization in the SnTe layer, as the thicker layers shift many of the reflectivity features to lower values of the scattering vector **Q**, where they can be more readily resolved. We note that magnetic proximity is expected to be stronger for a thicker CBST layer due to the higher T_c and larger magnetization moments associated with such a layer, so that the thicker layer may serve as a limiting upper bound of the proximity effect for the thinner samples used for transport. That is, any magnetization induced in the SnTe is expected to be weaker for the thinner samples studied through transport as compared to the thicker PNR sample.

We further note that the SnTe/CBST system suffers from an extremely poor nuclear scattering length density (SLD) contrast between the layers, with the experimentally determined SLD values of $2.031(5) \times 10^{-4-2}$ and $2.008(7) \times 10^{-4}$ nm^{-2}, respectively. To address this issue, we determined the thickness of the layers in different locations across the STEM specimen, and the PNR models were constrained accordingly. Figure 2c shows the measured reflectivity, and the inset is the spin asymmetry (SA) alongside a theoretical fit, where the SA is defined as the $(R^{\uparrow\uparrow} - R^{\downarrow\downarrow})/(R^{\uparrow\uparrow} + R^{\downarrow\downarrow})$. Here $R^{\uparrow\uparrow}$ and $R^{\downarrow\downarrow}$ represent the nonspin−flip reflectivities for neutrons aligned parallel or antiparallel to the applied magnetic field, respectively. It can clearly be seen that the fits are an excellent description of the data, and Figure 2d shows the theoretical model of the nuclear and magnetic SLD depth profiles used to generate the fits.

From this analysis, the thickness of the magnetized layer was determined to be 30.0 ± 0.4 nm (95% confidence interval), while the STEM-determined CBST thickness was 32.8 ± 1.9 nm (95% confidence interval). Both these 95% confidence intervals are shown in Figure 3c, illustrating that they do not quite overlap. We also consider an alternate model incorporating a magnetic proximity effect between SnTe and CBST. As shown in Figure S8, this model results in significantly worse fits to the data. The PNR and STEM thickness estimates combined with the magnetic depth profile conclusively demonstrate that the presence of a net in-plane magnetization does not extend beyond the CBST layer into SnTe, strongly arguing against the existence of a magnetic proximity effect. Note that while the combined STEM and PNR thickness information does support a small magnetically dead layer in the CBST at the interface, the dead layer may be as thin as a few angstroms and is on the edge of statistical

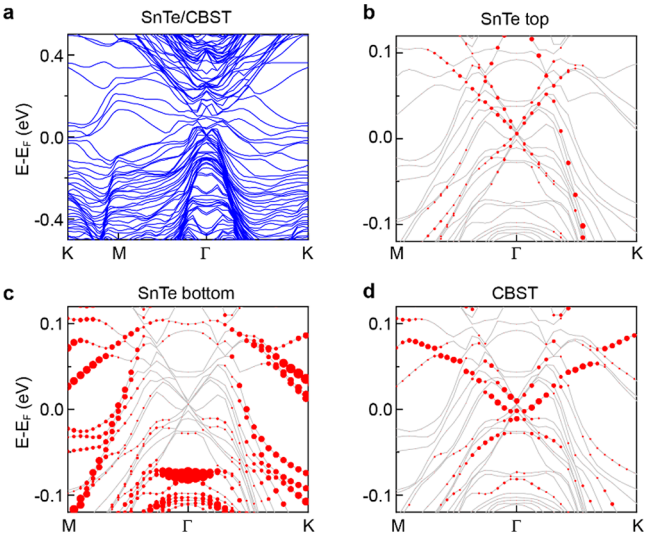

Figure 3. First-principles calculations of SnTe/CBST heterostructures. (a) Calculated band structure of a 21-BL-SnTe/2-QL-CBST heterostructure. (b−d) Projected band structures of (b) SnTe top 2-BL, (c) SnTe bottom 2-BL, and (d) CBST, respectively. Clear distinctions can be found between band contributions of the top and bottom surfaces, as a Dirac surface state is visible on SnTe top layer but is absent on SnTe bottom, indicating the surface state annihilation at the SnTe/CBST interface. Rather, additional surface state shows up in the gap of 2-QL-CBST.

significance. If real, a dead layer is likely attributable to a small amount of Cr migration away from or across the interface (Figure S2b). This may suppress the interfacial magnetization while not achieving sufficient Cr density to magnetize the SnTe.

We may further confirm the absence of a magnetic proximity effect by examining the transport properties of a SnTe/CBST heterostructure with a 1 QL thick $(BiSb)_2Te_3$ insertion layer in between (Figure S5). The undoped $(BiSb)_2Te_3$ layer separates the surface states of SnTe from the ferromagnetic order in CBST. As shown in Figure S5, this structure has the same signature of the ferromagnetic order as the sample without a $(BiSb)_2Te_3$ insertion layer. Moreover, the magnitude of the AHE is larger with the insertion layer, which is extremely unlikely to occur in the magnetic proximity effect scenario.

The surface state annihilation is also supported by the first-principles calculations. Figure 3a shows the calculated band structure of a 21-BL-SnTe/2-QL-CBST, while panels b−d of Figure 3 show the contributions from the SnTe top/bottom surface and CBST layers, respectively. Clear distinctions can be found between band contributions of SnTe top and bottom surfaces; i.e., a gapless Dirac surface state exists at the $\bar{\Gamma}$ point of the SnTe top surface (Figure 3b), whereas such a state is absent on the SnTe bottom surface (Figure 3c), due to the expected surface state annihilation at the interface. Moreover, we note that although the pristine 2-QL-CBST has a gap of 49.4 meV (Figure S10a), additional surface states show up in the CBST layer of the heterostructure (Figure 3d). To demonstrate the topologically nontrivial origin of these states, we further calculated the anomalous Hall conductivity of a 6-BL-SnTe/2-QL-CBST heterostructure. As shown in Figure S11, a large anomalous Hall conductivity is found at the Fermi level, clearly suggesting the existence of the nontrivial magnetic surface states.

https://doi.org/10.1021/acs.nanolett.2c00774
Nano Lett. 2022, 22, 5735−5741

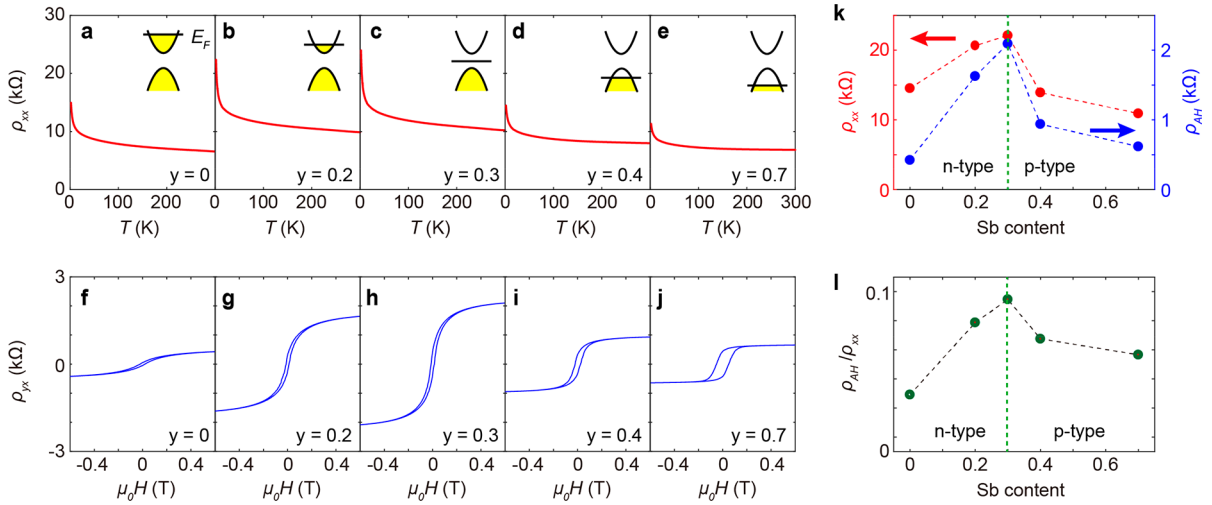

Figure 4. Tuning the Fermi levels of 9-BL-SnTe/2-QL-CBST heterostructures. (a–e) Temperature dependences of ρ_{xx} of 9-BL-SnTe/2-QL-$Cr_x(Bi_{1-y}Sb_y)_{2-x}Te_3$ samples with various Sb contents. (f–j) Field dependences of ρ_{yx} for the same samples. All curves are measured at 1.9 K. (k) Sb content dependences of ρ_{xx} and ρ_{AH}. (l) Sb content dependence of ρ_{AH}/ρ_{xx}.

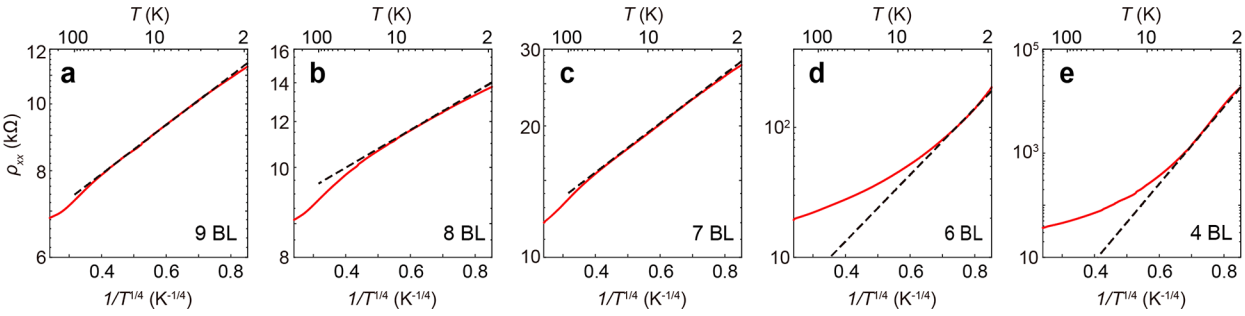

Figure 5. Tuning the thickness of the m-BL-SnTe/2-QL-CBST heterostructures. (a–e) Temperature dependences of ρ_{xx} for m-BL-SnTe/2-QL-CBST heterostructures with various SnTe thicknesses. The temperature range is between 1.9 and 300 K. Two distinct behaviors are observed between thick (m = 7–9) and thin (m = 4, 6) films. For thick films, the temperature-dependent ρ_{xx} can be fitted by a variable-range-hopping behavior as $\rho_{xx} \sim \exp[(T_0/T)^4]$ (black dashed lines), while the thin films are ill-fitted, suggesting a topological phase transition as the thickness is varied.

Next, we examine the magneto-transport response of the heterostructure to the tuning of Fermi level, which reveals the unique characteristics of nontrivial magnetic surface state. When the Fermi level is at the charge neutral point of CBST, both ρ_{xx} and the AH resistance (ρ_{AH}) should reach the maximum value,[34] owing to the minimized density of state and the maximized Berry curvature[35−38] at the point, respectively. Here, we grew a series of 9-BL-SnTe/2-QL-$Cr_x(Bi_{1-y}Sb_y)_{2-x}Te_3$ samples with varying Sb contents (y) ranging from y = 0 to y = 0.7. Since Bi_2Te_3 is n-type while Sb_2Te_3 is p-type,[39,40] the Fermi level can be systematically tuned as y varies,[41] as evidenced from the change in the sign of the Hall slope at high fields (Figure S6). Panels a–e of Figure 4 show the temperature dependence of ρ_{xx} for these samples. ρ_{xx} changes systematically, first becoming more resistive and then more conductive with increasing y. That the maximum of ρ_{xx} occurs at y = 0.3 corresponds to the point at which the Fermi level is tuned to the charge neutral point of CBST. Likewise, ρ_{AH} displays a trend similar to that in ρ_{xx}, first increasing then decreasing, reaching the maximum when y = 0.3 (Figure 4f–j). The evolutions of ρ_{xx} and ρ_{AH} and the tangent of the AH angle, ρ_{AH}/ρ_{xx}, are summarized in Figure 4k,l. All of these quantities show a dome-like dependence on Sb content with a maxima upon passing through the charge neutral point, such a response has also been reported in a pure CBST film.[34] This further suggests that the magnetic surface states are from CBST. Compared to CBST, the maxima of ρ_{xx} and ρ_{AH} occur at a much lower Sb content in the SnTe/CBST heterostructure owing to the p-type nature of SnTe.

Finally, we study the topological phase transition of the SnTe/CBST heterostructures. Due to the hybridization between the top and bottom surface states, a TI transitions into a trivial insulator as the thickness is reduced.[23−25,42,43] Figure 5 presents the temperature dependence of ρ_{xx} for a series of m-BL-SnTe/2-QL-CBST samples with the SnTe thickness, m, ranging from 4 to 9 BL. As the thickness decreases, samples become more resistive. More importantly, we observe a critical thickness that separates two regimes with two distinct behaviors of temperature-dependent ρ_{xx}. Above the critical thickness (7–9 BL), ρ_{xx} displays a linear relationship with $1/T^{1/4}$ over a wide temperature range at low temperatures in the Arrhenius plot (Figure 5a–c). Such a $\rho_{xx} \sim \exp[(T_0/T)^4]$ behavior has been commonly reported in TIs and may be ascribed to the variable-range-hopping mechanism.[44,45] On the other hand, below the critical thickness (4 and 6 BL), ρ_{xx} is ill-fitted by the $1/T^{1/4}$ law (Figure 5d,e). Rather, it may be better described by a thermally activated behavior $\rho_{xx} \sim \exp(T_0/T)$ (Figure S7), suggesting

https://doi.org/10.1021/acs.nanolett.2c00774
Nano Lett. 2022, 22, 5735−5741

the absence of the surface states in thin samples. Moreover, we note that the sample below the SnTe critical thickness is very insulating at low temperatures and becomes conductive abruptly at (and above) the critical thickness. This suggests that there exists no 2D electron gas due to the band alignment between CBST and SnTe, and the conduction channel originates from topological surface states. The abrupt change from variable-range-hopping to activated conduction between 7 and 6 BL samples is indicative of a phase transition from a TI to a trivial insulator as the thickness is reduced.[42,43]

In conclusion, by conducting magneto-transport and PNR measurements, as well as first-principles calculations, we demonstrated the annihilation and creation of topological surface states in SnTe/CBST heterostructures. Further, systematic changes in ρ_{xx} and ρ_{AH} are found as the Fermi level is tuned, showing the characteristics of the magnetic surface state. Finally, we revealed a topological phase transition in the heterostructure as the SnTe thickness is tuned. These findings offer a unique insight into manipulating and engineering the surface states in TIs, which are of great importance in the implementation of topological electronics. Different surface states have different properties such as spin texture, Fermi velocity, or localization length. With the proper choice of TIs and the stacking order, we could design new surface states by combining different symmetry-protected states into a TI heterostructure, offering a new avenue to realize dissipationless electronics.

MATERIALS AND METHODS

Sample Growth and Characterizations. The sample growth was conducted on a PerkinElmer MBE chamber with a base vacuum rate of 6.7×10^{-8} Pa. Prior to the growth, the epi-ready semi-insulating GaAs (111)B substrates were first degassed at 400 °C and then annealed under Te flux at 640 °C. High-purity Cr (99.995%), Bi (99.999%), Sn (99.9999%), and Te (99.9999%) were evaporated from standard Knudsen cells, and Sb (99.999%) was evaporated from a cracker cell. The growth temperature is about 200 °C for both CBST and SnTe. The flux ratio between Te and Bi/Sb is ∼10:1, while the flux ratio between Te and Sn is ∼50:1 during the growth of CBST and SnTe, respectively. For neutron and TEM experiments, samples were capped with a 2 nm thick Ti layer. The epitaxial growth was monitored by an in situ RHEED. The high-resolution XRD was performed using a PANalytical X'Pert Pro X-ray powder diffractometer with Cu Kα radiation (λ = 1.5406 Å).

Scanning Transmission Electron Microscopy. Cross-sectional specimens were prepared by the focused ion beam (FIB) lift-out using a Thermo-Fischer Nova NanoLab 600 system. Before lift-out, protective layers of sputtered carbon followed by ion beam deposited Pt−C were applied to the surface of the thin film. High-resolution STEM experiments were then performed using a Thermo-Fischer Titan 80−300 keV (S)TEM instrument operating with a primary beam energy of 300 keV. EELS was performed on a Gatan spectrometer, with a convergence angle of 13.7 mrad and a collection angle of 22 mrad, 0.2 eV/channel dispersion with 1 eV energy resolution, and a 40 ms dwell time. XEDS was taken with an EDAX r-TEM X-ray energy dispersive spectrometer, with a convergence angle of 24 mrad and 0.5 s dwell time. Scanning nanobeam electron diffraction measurements were taken with a Merlin Medipix 3RX from Quantum Detectors with a 0.5 mrad convergence angle and a 2 ms dwell time.

Device Fabrication and Transport Measurement. The MBE-grown films were fabricated into Hall bars using hard masks and reactive-ion etching with CHF_3. The effective region of the Hall bar is 1 × 0.5 mm^2. The transport measurement was carried out on a commercial PPMS (1.9 K, 9 T). For resistance measurements of samples with reasonable conductance, a 1 μA AC excitation current and standard lock-ins were used. For very insulating samples (>500 kΩ), a 1 μA DC excitation current was applied. The anomalous Hall resistance has been antisymmetrized.

Polarized Neutron Reflectometry. PNR measurements were performed using the PBR instrument at the NIST Center for Neutron Research. Incident neutrons were spin-polarized parallel or antiparallel to the applied magnetic field. The nonspin−flip reflectivities, in which the incident and scattered neutron have the same spin direction, were collected as a function of wave-vector transfer ($\mathbf{Q}$) along the film normal. The PNR measurements were performed at 5 K with an in-plane applied field of 3 T. Data were reduced using the Reductus software package and fit using the Refl1D software package using a differential evolution method for parameter optimization and a Markov chain Monte Carlo algorithm for uncertainty analysis, as implemented in the BUMPS python package.

First-Principles Calculations. The first-principles calculations were performed by using the projected augmented-wave method as implemented in the Vienna ab initio simulation package (VASP). The generalized gradient approximation (GGA) of the Perdew−Burke−Ernzerhof type was utilized to treat the exchange−correlation interaction. In our calculations, a 2 × 2 supercell was used to simulate the experimental CBST doping concentration of $(Cr_{0.125}Bi_{0.25}Sb_{0.625})_2Te_3$. The dangling bond of Te-terminated SnTe(111) surface was passivated with Na atoms. We used the number of the Sn layer as the number of BL. The DFT-D2 method was used to describe the van der Waals interaction of the heterostructure. During structural optimization, the atoms of CBST, and SnTe from the outmost four atomic layers were allowed to move whereas the interior atoms of SnTe were fixed. The kinetic energy cutoff, energy convergence threshold and Hellmann−Feynman force tolerance criterion were set to be 520 eV, 10^{-5} eV and 0.01 eV/Å, respectively. A Γ-centered 5 × 5 × 1 k mesh was adopted. The 3d states of Cr were treated with GGA+U approach, with U = 3.0 eV and J = 0.87 eV. The anomalous Hall conductivity was calculated by constructing a maximally localized Wannier function as implemented in the Wannier90 package.

ASSOCIATED CONTENT

Supporting Information

The Supporting Information is available free of charge at https://pubs.acs.org/doi/10.1021/acs.nanolett.2c00774.

Nanobeam electron diffraction characterizations; STEM spectroscopy, XRD, and transport results; heterostructure with a nonmagnetic insertion layer; change of carrier type; Arrhenius plots; polarized neutron reflectometry analysis; calculated band structures and anomalous Hall conductance (PDF)

https://doi.org/10.1021/acs.nanolett.2c00774
Nano Lett. 2022, 22, 5735−5741

AUTHOR INFORMATION

Corresponding Authors

Peng Deng − *Department of Electrical and Computer Engineering, University of California, Los Angeles, California 90095, United States; Beijing Academy of Quantum Information Science, Beijing 100193, China*; Email: dengpeng@g.ucla.edu

Zhenhua Qiao − *NIST Center for Neutron Research, National Institute of Standards and Technology, Maryland 20899-6102, United States*; Email: qiao@ustc.edu.cn

Kang L. Wang − *Department of Electrical and Computer Engineering and Department of Physics and Astronomy, University of California, Los Angeles, California 90095, United States*; orcid.org/0000-0003-0487-5464; Email: wang@ee.ucla.edu

Authors

Alexander Grutter − *NIST Center for Neutron Research, National Institute of Standards and Technology, Maryland 20899-6102, United States*; orcid.org/0000-0002-6876-7625

Yulei Han − *ICQD, Hefei National Laboratory for Physical Sciences at Microscale, CAS Key Laboratory of Strongly-Coupled Quantum Matter Physics, and Department of Physics, University of Science and Technology of China, Anhui 230026, China*

Megan E. Holtz − *Materials Measurement Laboratory, National Institute of Standards and Technology, Maryland 20899-6102, United States*

Peng Zhang − *Department of Electrical and Computer Engineering, University of California, Los Angeles, California 90095, United States*

Patrick Quarterman − *NIST Center for Neutron Research, National Institute of Standards and Technology, Maryland 20899-6102, United States*

Shuaihang Pan − *Department of Mechanical and Aerospace Engineering, University of California, Los Angeles, California 90095, United States*; orcid.org/0000-0002-5312-992X

Shifei Qi − *College of Physics and Hebei Advanced Thin Film Laboratory, Hebei Normal University, Hebei 050024, China; ICQD, Hefei National Laboratory for Physical Sciences at Microscale, CAS Key Laboratory of Strongly-Coupled Quantum Matter Physics, and Department of Physics, University of Science and Technology of China, Anhui 230026, China*

Complete contact information is available at: https://pubs.acs.org/10.1021/acs.nanolett.2c00774

Author Contributions

P.D., A.G., and Y.H. contributed equally to this work. P.D., Z.Q., and K.L.W. conceived the research project. K.L.W. supervised the project. P.D. and P.Z. grew the sample. S.P. performed XRD measurements. M.E.H. performed the STEM, EELS, and XEDS experiments. P.D. and P.Z. fabricated the devices and performed the transport experiments. A.G. and P.Q. performed the neutron experiments and analyses. Y.H., S.Q., and Z.Q. performed theoretical calculations. P.D., A.G., YH., Z.Q., and K.L.W. wrote the manuscript with inputs from all authors.

Notes

The authors declare no competing financial interest.

ACKNOWLEDGMENTS

This work is partially supported by the Spins and Heat in Nanoscale Electronic Systems (SHINES) Center funded by the U.S. Department of Energy (DOE) under Award No. DE-SC0012670, the U.S. Army Research Office MURI program under Grants No. W911NF-16-1-0472, and the NSF Grant Nos. DMR-1810163 and EEC-1160504. This work is partially supported by the NNSFC (Grant Nos. 11974098, 11974327, and 12004369), Fundamental Research Funds for the Central Universities (Grant Nos. WK2030020032 and WK2340000082), and Anhui Initiative in Quantum Information Technologies. The Supercomputing services of AM-HPC and USTC are gratefully acknowledged. The research was performed in part at the NIST Center for Nanoscale Science and Technology. Certain commercial equipment, instruments, or materials are identified in this paper to foster understanding. Such identification does not imply recommendation or endorsement by the National Institute of Standards and Technology, nor does it imply that the materials or equipment identified are necessarily the best available.

REFERENCES

(1) Hasan, M. Z.; Kane, C. L. Colloquium: topological insulators. *Rev. Mod. Phys.* **2010**, *82* (4), 3045.

(2) Qi, X.-L.; Zhang, S.-C. Topological insulators and superconductors. *Rev. Mod. Phys.* **2011**, *83* (4), 1057.

(3) Rauch, T.; Flieger, M.; Henk, J.; Mertig, I. Nontrivial interface states confined between two topological insulators. *Phys. Rev. B* **2013**, *88* (24), 245120.

(4) Mogi, M.; Yoshimi, R.; Tsukazaki, A.; Yasuda, K.; Kozuka, Y.; Takahashi, K.; Kawasaki, M.; Tokura, Y. Magnetic modulation doping in topological insulators toward higher-temperature quantum anomalous Hall effect. *Appl. Phys. Lett.* **2015**, *107* (18), 182401.

(5) Deng, H.; Chen, Z.; Wołoś, A.; Konczykowski, M.; Sobczak, K.; Sitnicka, J.; Fedorchenko, I. V.; Borysiuk, J.; Heider, T.; Pluciński, Ł.; et al. High-temperature quantum anomalous Hall regime in a MnBi2Te4/Bi2Te3 superlattice. *Nat. Phys.* **2021**, *17* (1), 36−42.

(6) Mogi, M.; Okamura, Y.; Kawamura, M.; Yoshimi, R.; Yasuda, K.; Tsukazaki, A.; Takahashi, K.; Morimoto, T.; Nagaosa, N.; Kawasaki, M.; et al. Experimental signature of the parity anomaly in a semimagnetic topological insulator. *Nat. Phys.* **2022**, *18*, 390−394.

(7) Yasuda, K.; Wakatsuki, R.; Morimoto, T.; Yoshimi, R.; Tsukazaki, A.; Takahashi, K.; Ezawa, M.; Kawasaki, M.; Nagaosa, N.; Tokura, Y. Geometric Hall effects in topological insulator heterostructures. *Nat. Phys.* **2016**, *12* (6), 555−559.

(8) Jiang, J.; Xiao, D.; Wang, F.; Shin, J.-H.; Andreoli, D.; Zhang, J.; Xiao, R.; Zhao, Y.-F.; Kayyalha, M.; Zhang, L.; et al. Concurrence of quantum anomalous Hall and topological Hall effects in magnetic topological insulator sandwich heterostructures. *Nat. Mater.* **2020**, *19* (7), 732−737.

(9) Liu, J.; Singh, A.; Liu, Y. Y. F.; Ionescu, A.; Kuerbanjiang, B.; Barnes, C. H.; Hesjedal, T. Exchange Bias in Magnetic Topological Insulator Superlattices. *Nano Lett.* **2020**, *20* (7), 5315−5322.

(10) Kane, C. L.; Mele, E. J. Z 2 topological order and the quantum spin Hall effect. *Phys. Rev. Lett.* **2005**, *95* (14), 146802.

(11) Fu, L.; Kane, C. L.; Mele, E. J. Topological insulators in three dimensions. *Phys. Rev. Lett.* **2007**, *98* (10), 106803.

(12) Zhang, H.; Liu, C.-X.; Qi, X.-L.; Dai, X.; Fang, Z.; Zhang, S.-C. Topological insulators in Bi 2 Se 3, Bi 2 Te 3 and Sb 2 Te 3 with a single Dirac cone on the surface. *Nat. Phys.* **2009**, *5* (6), 438−442.

(13) Xia, Y.; Qian, D.; Hsieh, D.; Wray, L.; Pal, A.; Lin, H.; Bansil, A.; Grauer, D.; Hor, Y. S.; Cava, R. J.; et al. Observation of a large-gap topological-insulator class with a single Dirac cone on the surface. *Nat. Phys.* **2009**, *5* (6), 398−402.

(14) Fu, L. Topological crystalline insulators. *Phys. Rev. Lett.* **2011**, *106* (10), 106802.

(15) Hsieh, T. H.; Lin, H.; Liu, J.; Duan, W.; Bansil, A.; Fu, L. Topological crystalline insulators in the SnTe material class. *Nat. Commun.* **2012**, *3* (1), 982.
(16) Tanaka, Y.; Ren, Z.; Sato, T.; Nakayama, K.; Souma, S.; Takahashi, T.; Segawa, K.; Ando, Y. Experimental realization of a topological crystalline insulator in SnTe. *Nat. Phys.* **2012**, *8* (11), 800−803.
(17) Dziawa, P.; Kowalski, B.; Dybko, K.; Buczko, R.; Szczerbakow, A.; Szot, M.; Łusakowska, E.; Balasubramanian, T.; Wojek, B. M.; Berntsen, M.; et al. Topological crystalline insulator states in Pb1-xSnxSe. *Nat. Mater.* **2012**, *11* (12), 1023−1027.
(18) Xu, S.-Y.; Liu, C.; Alidoust, N.; Neupane, M.; Qian, D.; Belopolski, I.; Denlinger, J.; Wang, Y.; Lin, H.; Wray, L. a.; et al. Observation of a topological crystalline insulator phase and topological phase transition in Pb1- xSnxTe. *Nat. Commun.* **2012**, *3* (1), 1192.
(19) Tanaka, Y.; Shoman, T.; Nakayama, K.; Souma, S.; Sato, T.; Takahashi, T.; Novak, M.; Segawa, K.; Ando, Y. Two types of Dirac-cone surface states on the (111) surface of the topological crystalline insulator SnTe. *Phys. Rev. B* **2013**, *88* (23), 235126.
(20) Takahashi, R.; Murakami, S. Gapless interface states between topological insulators with opposite Dirac velocities. *Phys. Rev. Lett.* **2011**, *107* (16), 166805.
(21) Habe, T.; Asano, Y. Robustness of gapless interface states in a junction of two topological insulators. *Phys. Rev. B* **2013**, *88* (15), 155442.
(22) Huang, H.; Wang, Z.; Luo, N.; Liu, Z.; Lü, R.; Wu, J.; Duan, W. Time-reversal symmetry protected chiral interface states between quantum spin and quantum anomalous Hall insulators. *Phys. Rev. B* **2015**, *92* (7), 075138.
(23) Liu, C.-X.; Zhang, H.; Yan, B.; Qi, X.-L.; Frauenheim, T.; Dai, X.; Fang, Z.; Zhang, S.-C. Oscillatory crossover from two-dimensional to three-dimensional topological insulators. *Phys. Rev. B* **2010**, *81* (4), 041307.
(24) Lu, H.-Z.; Shan, W.-Y.; Yao, W.; Niu, Q.; Shen, S.-Q. Massive Dirac fermions and spin physics in an ultrathin film of topological insulator. *Phys. Rev. B* **2010**, *81* (11), 115407.
(25) Linder, J.; Yokoyama, T.; Sudbø, A. Anomalous finite size effects on surface states in the topological insulator Bi 2 Se 3. *Phys. Rev. B* **2009**, *80* (20), 205401.
(26) Taskin, A.; Yang, F.; Sasaki, S.; Segawa, K.; Ando, Y. Topological surface transport in epitaxial SnTe thin films grown on Bi 2 Te 3. *Phys. Rev. B* **2014**, *89* (12), 121302.
(27) Yan, C.; Liu, J.; Zang, Y.; Wang, J.; Wang, Z.; Wang, P.; Zhang, Z.-D.; Wang, L.; Ma, X.; Ji, S.; et al. Experimental observation of Dirac-like surface states and topological phase transition in Pb1-xSnxTe (111) films. *Phys. Rev. Lett.* **2014**, *112* (18), 186801.
(28) Wang, F.; Zhang, H.; Jiang, J.; Zhao, Y.-F.; Yu, J.; Liu, W.; Li, D.; Chan, M. H.; Sun, J.; Zhang, Z.; et al. Chromium-induced ferromagnetism with perpendicular anisotropy in topological crystalline insulator SnTe (111) thin films. *Phys. Rev. B* **2018**, *97* (11), 115414.
(29) Jiang, Y.; Wang, Y.; Chen, M.; Li, Z.; Song, C.; He, K.; Wang, L.; Chen, X.; Ma, X.; Xue, Q.-K. Landau quantization and the thickness limit of topological insulator thin films of Sb 2 Te 3. *Phys. Rev. Lett.* **2012**, *108* (1), 016401.
(30) Wei, P.; Katmis, F.; Assaf, B. A.; Steinberg, H.; Jarillo-Herrero, P.; Heiman, D.; Moodera, J. S. Exchange-coupling-induced symmetry breaking in topological insulators. *Phys. Rev. Lett.* **2013**, *110* (18), 186807.
(31) Katmis, F.; Lauter, V.; Nogueira, F. S.; Assaf, B. A.; Jamer, M. E.; Wei, P.; Satpati, B.; Freeland, J. W.; Eremin, I.; Heiman, D.; et al. A high-temperature ferromagnetic topological insulating phase by proximity coupling. *Nature* **2016**, *533* (7604), 513−516.
(32) Tang, C.; Chang, C.-Z.; Zhao, G.; Liu, Y.; Jiang, Z.; Liu, C.-X.; McCartney, M. R.; Smith, D. J.; Chen, T.; Moodera, J. S.; et al. Above 400-K robust perpendicular ferromagnetic phase in a topological insulator. *Sci. Adv.* **2017**, *3* (6), No. e1700307.
(33) He, Q. L.; Kou, X.; Grutter, A. J.; Yin, G.; Pan, L.; Che, X.; Liu, Y.; Nie, T.; Zhang, B.; Disseler, S. M.; et al. Tailoring exchange couplings in magnetic topological-insulator/antiferromagnet heterostructures. *Nat. Mater.* **2017**, *16* (1), 94−100.
(34) Chang, C. Z.; Zhang, J.; Liu, M.; Zhang, Z.; Feng, X.; Li, K.; Wang, L. L.; Chen, X.; Dai, X.; Fang, Z.; et al. Thin films of magnetically doped topological insulator with carrier-independent long-range ferromagnetic order. *Adv. Mater.* **2013**, *25* (7), 1065−1070.
(35) Nagaosa, N.; Sinova, J.; Onoda, S.; MacDonald, A. H.; Ong, N. P. Anomalous hall effect. *Rev. Mod. Phys.* **2010**, *82* (2), 1539.
(36) Fang, Z.; Nagaosa, N.; Takahashi, K. S.; Asamitsu, A.; Mathieu, R.; Ogasawara, T.; Yamada, H.; Kawasaki, M.; Tokura, Y.; Terakura, K. The anomalous Hall effect and magnetic monopoles in momentum space. *Science* **2003**, *302* (5642), 92−95.
(37) Haldane, F. Berry curvature on the Fermi surface: anomalous Hall effect as a topological Fermi-liquid property. *Phys. Rev. Lett.* **2004**, *93* (20), 206602.
(38) Nomura, K.; Nagaosa, N. Surface-quantized anomalous Hall current and the magnetoelectric effect in magnetically disordered topological insulators. *Phys. Rev. Lett.* **2011**, *106* (16), 166802.
(39) Chen, Y.; Analytis, J. G.; Chu, J.-H.; Liu, Z.; Mo, S.-K.; Qi, X.-L.; Zhang, H.; Lu, D.; Dai, X.; Fang, Z.; et al. Experimental realization of a three-dimensional topological insulator, Bi2Te3. *Science* **2009**, *325* (5937), 178−181.
(40) Hsieh, D.; Xia, Y.; Qian, D.; Wray, L.; Meier, F.; Dil, J.; Osterwalder, J.; Patthey, L.; Fedorov, A.; Lin, H.; et al. Observation of time-reversal-protected single-Dirac-cone topological-insulator states in Bi2Te3 and Sb2Te3. *Phys. Rev. Lett.* **2009**, *103* (14), 146401.
(41) Zhang, J.; Chang, C.-Z.; Zhang, Z.; Wen, J.; Feng, X.; Li, K.; Liu, M.; He, K.; Wang, L.; Chen, X.; et al. Band structure engineering in (Bi 1- x Sb x) 2 Te 3 ternary topological insulators. *Nat. Commun.* **2011**, *2* (1), 574.
(42) Liu, J.; Fu, L. Electrically tunable quantum spin Hall state in topological crystalline insulator thin films. *Phys. Rev. B* **2015**, *91* (8), 081407.
(43) Safaei, S.; Galicka, M.; Kacman, P.; Buczko, R. Quantum spin Hall effect in IV-VI topological crystalline insulators. *New J. Phys.* **2015**, *17* (6), 063041.
(44) Ren, Z.; Taskin, A.; Sasaki, S.; Segawa, K.; Ando, Y. Optimizing Bi 2- x Sb x Te 3- y Se y solid solutions to approach the intrinsic topological insulator regime. *Phys. Rev. B* **2011**, *84* (16), 165311.
(45) Skinner, B.; Chen, T.; Shklovskii, B. Why is the bulk resistivity of topological insulators so small? *Phys. Rev. Lett.* **2012**, *109* (17), 176801.

https://doi.org/10.1021/acs.nanolett.2c00774
Nano Lett. 2022, 22, 5735−5741